Nanoscale

ROYAL SOCIETY OF CHEMISTRY

PAPER

View Article Online
View Journal | View Issue

Cite this: *Nanoscale*, 2020, **12**, 11153

Injectable DNA-architected nanoraspberry depot-mediated on-demand programmable refilling and release drug delivery†

Ru-Siou Hsu,[a] Jen-Hung Fang,[a] Wei-Ting Shen,[a] Yu-Chen Sheu,[a] Cheng-Kuan Su,[b] Wen-Hsuan Chiang [c] and Shang-Hsiu Hu *[a]

Received 11th February 2020,
Accepted 2nd May 2020

DOI: 10.1039/d0nr01185a

rsc.li/nanoscale

Drug delivery depots boosting a local concentration of therapeutic agents have received great attention in clinical applications due to their low occurrence of side effects and high therapeutic efficacy. However, once the payload is exhausted, the local drug concentration will be lower than the therapeutic window. To address this issue, an injectable double-strand deoxyribonucleic acid (DNA)-architected nanoraspberry depot (DNR-depot) was developed that can refill doxorubicin (Dox, an anticancer drug) from the blood and remotely control drug release on demand. The large porous surface on a uniform nanoraspberry (NR) filled covalently with DNA serves as a Dox sponge-like refilling reservoir, and the NR serves as a magnetic electrical absorber. *Via* the strong affinity between Dox and DNA molecules, the refilling process of Dox can be achieved on DNR-depot both *in vitro* and *in vivo*. Upon high-frequency magnetic field (HFMF) treatment, the remotely triggered release of Dox is actuated by the dissociation of Dox and DNA molecules, facilitating an approximately 800% improvement in drug concentration at the tumor site compared to free Dox injection alone. Furthermore, the cycles of refilling and release can be carried out more than 3 times *in vivo* within 21 days. The combination of refilling and HFMF-programmable Dox release in tumors *via* DNR-depot can effectively inhibit tumor growth for 30 days.

Introduction

Advanced local drug delivery systems, including polymer-based depots,[1–4] nanoparticle drug reservoirs[5,6] and macroscale complexes[7,8] provide promising strategies for improving controlled drug release and immunotherapy in the clinic. The major proposals of these local depots are designed to solve off-target toxicity and minimize excessive drug dosing. Such drugs that locally release over a longer period of time can also enhance compliance for elderly or noncompliant patients. In the clinic, the local chemotherapeutic Gliadel wafer (an FDA-approved local delivery device) or brachytherapy (a point-source radiation seed) implanted surrounding the postoperative wound have served as adjuvants to surgery to avoid locoregional recurrence after tumor resection, which also protect against the progression of disseminated metastatic cancer cells, especially for early-stage cancers.[9,10] Furthermore, other versatile devices performing programmed drug release *via* the integration of electronic engineering, computing and machinery science for medical equipment for precise drug release have also been developed.[11–15] Overall, local drug delivery depots are potentially applied at each stage of cancer for curative or palliative intent to improve existing approaches.

Despite recent advances in drug delivery depots, only a few biodegradable depots (polymeric-based materials) possess the function of on-demand drug release, and most release relies on diffusion or pH or enzymatic cleavage to degrade the materials.[16] Thus, it is difficult to maintain the local concentrations of therapeutic agents, lowering the therapeutic efficacy. Furthermore, the microenvironments surrounding implanted depots vary among individual patients or diseases, leading to difficulties in predicting the *a priori* therapeutic window and release kinetics of the drug. For this situation, on-demand drug release is critical to manage the drug dosage. In this regard, stimuli-responsive biodegradable depots displaying on-demand drug release demonstrate promising enhancement in various treatments,[17,18] where programmable drug release can be managed in real time at a suitable dose by external physical energy, such as ultrasound, electricity, light and magnetic fields.[19,20] For example, capsules constructed by

[a]*Department of Biomedical Engineering and Environmental Sciences, National Tsing Hua University, Hsinchu, 300, Taiwan. E-mail: shhu@mx.nthu.edu.tw*
[b]*Department of Chemistry, National Chung Hsing University, Taichung 402, Taiwan*
[c]*Department of Chemical Engineering, National Chung Hsing University, Taichung 402, Taiwan*

†Electronic supplementary information (ESI) available. See DOI: 10.1039/d0nr01185a

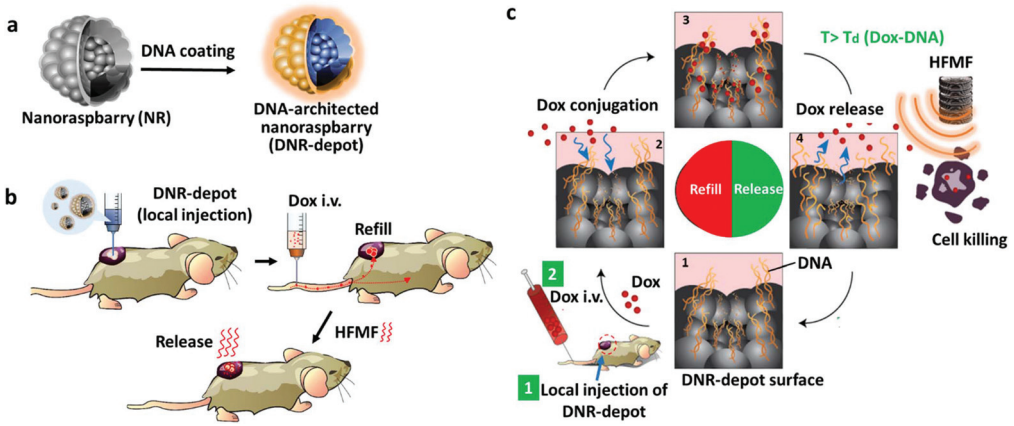

Fig. 1 (a) Schematic representation of the injectable DNA-architected nanoraspberry depot (DNR-depot) serving as a Dox sponge-like refilling reservoir and magnetothermal converter. (b) The process of DNR-depot-mediated local drug refilling and release at the tumor site. (i) Intratumoral injection of DNR-depot, (ii) intravenous (i.v.) injection of Dox, and (iii) HFMF treatment. (c) The cycle of refilling and release of the DNR-depot. Dox conjugated on DNR-depot for refilling and magnetothermal heating induced the disassembly of the DNA for Dox release.

hydrogels have revealed a faster drug release pattern under ultrasonic stimulus by loosening the molecular structures.[21] In addition, an external high-frequency magnetic field (HFMF) has also been applied to trigger rapid drug release from nanocapsules composed of magnetic particles and proteins.[22] However, these stimulus-responsive drug delivery systems cannot refill drugs *in vivo* for long-term use.

Recently, a new strategy for "refilling" local drug delivery systems has been developed to reload fresh drug molecules (anticancer drugs) into devices through blood circulation.[23] This approach *via* intravenous injection (i.v.) imposes the merit of trapping the drugs at the target site and reducing toxicity to the clearance organs and other tissues. For example, using an alginate modified with oligodeoxynucleotides (ODNs), Brudno and coworkers constructed an intratumorally injected local device as a target site to specifically bind other complementary ODNs conjugated to oxidized alginate strands.[24] This ODN-alginate device displayed 5-fold greater drug binding than the control gel group. After four refilling cycles of *in vivo* of complementary-ODN-loaded doxorubicin (Dox), tumor inhibition was clearly observed compared with traditional administration and other nonrefilling systems.

Based on metabolic glycoengineering and click chemistry, the refilling drug delivery system was constructed by combining nanoparticles and metabolic glycoengineering.[25] First, azide groups were generated on the tumor cell surface (A549 human lung cancer cells) by metabolic glycoengineering of particles at the tumor. Then, bicyclo[6.1.0]nonyne (BCN)-modified particles with the targeted photosensitizer chlorin e6 (Ce6) were bound to the azide groups on tumor cells *via* click chemistry for photodynamic therapy. Through this strategy, the concentration of photosensitizer (Ce6) was 10-fold higher than free Ce6 administration. Furthermore, the gel-based refilling system modified by the sugar backbone was able to locally capture the Tz radioprobe. This gel improved the level of radioactivity at the target site.[26] These works indicated that this refilling system could be a new tool for the control of local delivery, potentially substituting for traditional targeting *via* specific biochemical conjunctions.[27,28]

Here, an injectable DNA-architected nanoraspberry depot (DNR-depot) that serves as a Dox sponge-like refilling reservoir as well as a magnetothermal converter to amplify the local concentration of therapeutic agents was developed (Fig. 1a). Being magneto-responsive, this DNR-depot is able to locally capture fresh anticancer drugs (such as doxorubicin, Dox) and exhibits superior triggered release upon stimulation from a high-frequency magnetic field (HFMF). As shown in Fig. 1b, the DNR-depot was implanted at the tumor site through intratumoral injection. Then, the refilling process was achieved by intravenous injection of Dox within a few minutes, where the effective refilling of fresh Dox into DNR-depot was realized by the strong affinity between Dox and DNA molecules from a large volume of Dox sponge-like refilling reservoir (Fig. 1c). Upon subjecting the tumor to a high-frequency magnetic field (HFMF), the magnetothermal conversion of the DNR-depot led to intense heat to temporarily break the hydrogen bonds of DNA, resulting in drug release. The robust and programmable cycles of refilling and release can repeatedly suppress tumor cells by enhancing the local drug concentration.

Results and discussion

The nanoraspberry (NR), a porous iron oxide particle, was prepared through a robust ligand-aided synthetic approach by applying oleic amine (OA) and sodium citrate as coordinating agents in a hydrothermal reaction.[29] As shown in Fig. 2a, NRs with a diameter of approximately 100 nm were observed after 4 h of hydrothermal reaction at 220 °C. Higher magnification SEM images showed that the particles had few pores on the surface and were composed of several particle domains (Fig. 2b). With increasing reaction time to 10 h, the size of NR increased to 130 nm and maintained a uniform particle size distribution (Fig. 2c). Furthermore, additional particle

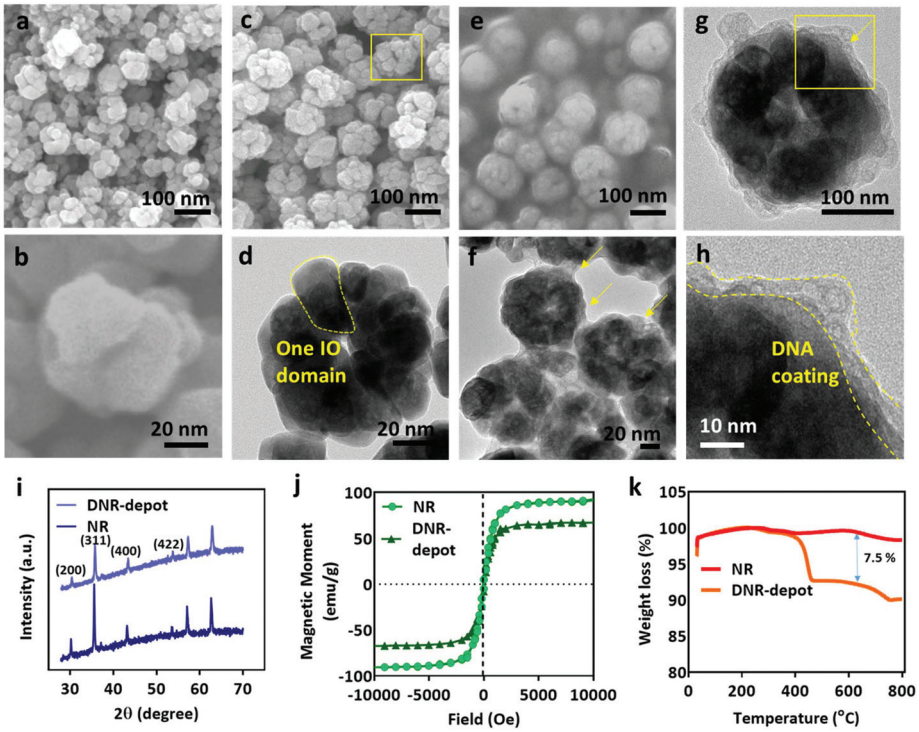

Fig. 2 SEM images of the NRs fabricated for (a and b) 4 h and (c) 10 h of hydrothermal treatment at 220 °C. (d) TEM image of a NR. (e) SEM image and (f–h) TEM images of DNR-depot. (i) X-ray diffraction patterns, (j) field-dependent magnetization curve, and (k) thermogravimetric analysis (TGA) analysis of the as-synthesized NR and DNR-depot.

domains and pores were observed in one NR, as exhibited in the TEM image (Fig. 2d). To evaluate the surface area, the Brunauer–Emmett–Teller (BET) method was applied to measure gas absorption isotherms (N_2) at 77 K, and the pore-size distribution was also determined through the Barrett, Joyner and Halenda (BJH) method. The particles were treated at 80 °C under vacuum to remove the surface adsorption and were degassed at 180 °C for 4 h before BET analysis. The results revealed that each NR had a surface area of ~186 m^2 g^{-1} and a pore size of ~13 nm (see Fig. S1a and S1b in ESI†). The DNR exhibited a reduced surface area and smaller pore size than the NR owing to the DNA coating on NR. However, after 24 h of reaction, random growth of domains in the NR were observed (see ESI, Fig. S1c and S1d†). Formation of the porous structure was potentially induced by the nucleation and growth of iron salts in ethylene glycol through the oriented growth of primary iron oxide nucleation, and the orientation minimized the surface energy. In the reaction, oleic acid (OA) was applied as a surfactant to restrict the growth of iron oxide, facilitating the generation of porous structures and causing the hydrophobicity of the NR. Regarding the size distribution and porosity, 10 h of NR hydrothermal reaction at 220 °C was applied for further use.

The OA-capped NR was then covalently conjugated to DNA through the 5′-end specificity of oligonucleotide attachment by the EDC reaction (see ESI, Fig. S2†).[30] During the reaction, the EDC-activated phosphate group forms an intermediate, and then the imidazole molecule attacks the intermediate to form a reactive phosphoryl imidazoline, which is a longer-lived intermediate. Finally, the primary amine on the NR surface reacts with phosphoryl imidazoline to create the DNR-depot. The SEM images of the resulting DNR-depot in Fig. 2e showed the smooth surface of the particles, indicating DNA deposition onto the NRs. After DNA coating, the TEM image showed that the resulting particle with a thin layer of DNA on the NR was only a few nanometers thick (Fig. 2f–h). Furthermore, no obvious cracks were observed on the DNR-depot, indicating a good interface between the two materials.

In Fig. 2i, the X-ray diffraction (XRD) patterns display major diffraction peaks that are characteristic of the Fe_3O_4 crystal plane according to the JCPDS [85-1436]. DNR-depot revealed characteristic peaks with weaker diffraction than those of the NR because of the presence of amorphous DNA on the NR. Furthermore, a superconducting quantum interference device (SQUID) was used to determine the magnetic properties of the NR and DNR-depot (Fig. 2j). Both the NR and DNR-depot exhibited a nearly identical shape and negligible hysteresis. A lower saturation magnetization (M_s) of DNR-depot also reflected the organic coating on the NR. Moreover, thermogravimetric analysis (TGA) of the NR and DNR-depot further showed the DNA conjugation ratio to NR, with approximately 7.5% weight loss from DNA (Fig. 2k).

The chemical bonds between the NR and DNA were evaluated by X-ray photoelectron spectroscopy (XPS, Fig. 3). After DNA conjugation, a peak at 288 eV (C 1s) for amide bonds (O═C–N) was observed, which represented the formation of

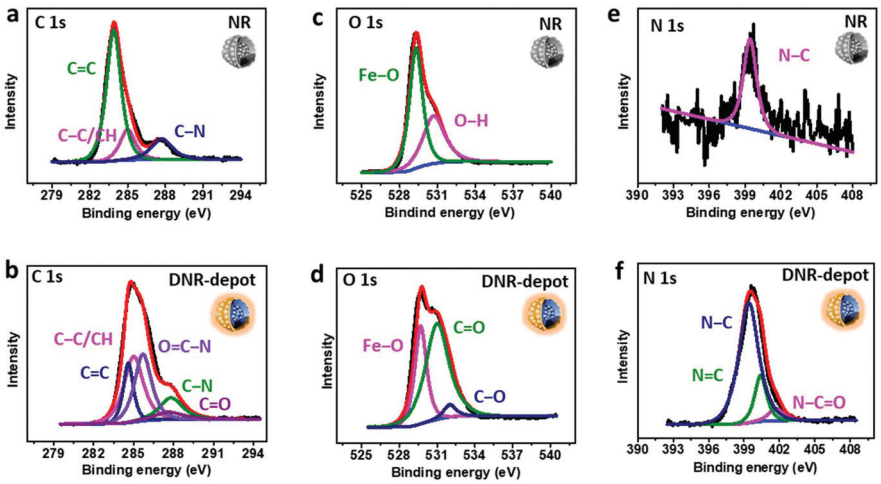

Fig. 3 XPS survey scan spectra of (a and b) C 1s, (c and d) O 1s and (e and f) N 1s of NRs and DNR-depot.

bonds between the NR and DNA (Fig. 3a and b). Furthermore, the binding energy of the O 1s (527.0 to 537.0 eV) of NR and DNR-depot was measured. The O 1s peak of NR was mainly at 529.3 eV. While DNA and NR were incorporated, an obvious shift to a higher energy position, *i.e.*, 531.3 eV, was detected, indicating that a carboxylic acid was chemically immobilized onto the NR. The bonding energy of the N 1s also further confirmed the incorporation of DNA onto the NR through the observation of N–C═O bonding (Fig. 3e and f). The higher binding energy was potentially attributed to the conjugation of the EDC reaction between the amine of NR and DNA, which formed solid networking covalent bonds.

When 20 μg mL^{-1} DNR-depot and NR were subjected to HFMF for 120 s, a rapid increase in temperature was observed, as shown in Fig. 4a. Within one minute, the temperature of the solution containing 1% DNR-depot increased to 60 °C. The mechanism of HFMF inducing heat *via* magnetic particles was caused by the energy dissipation, known as Brown and Néel relaxations.[31,32] The magnetic domain and particle size also affected the heating rate. Compared to single-domain magnetic particles, the multiple domains of NR exhibited a more efficient induction of heat due to the higher internal energy of dissipation between each domain.[33] Even when the concentration of DNR-depot was 10 μg mL^{-1}, the local temperature

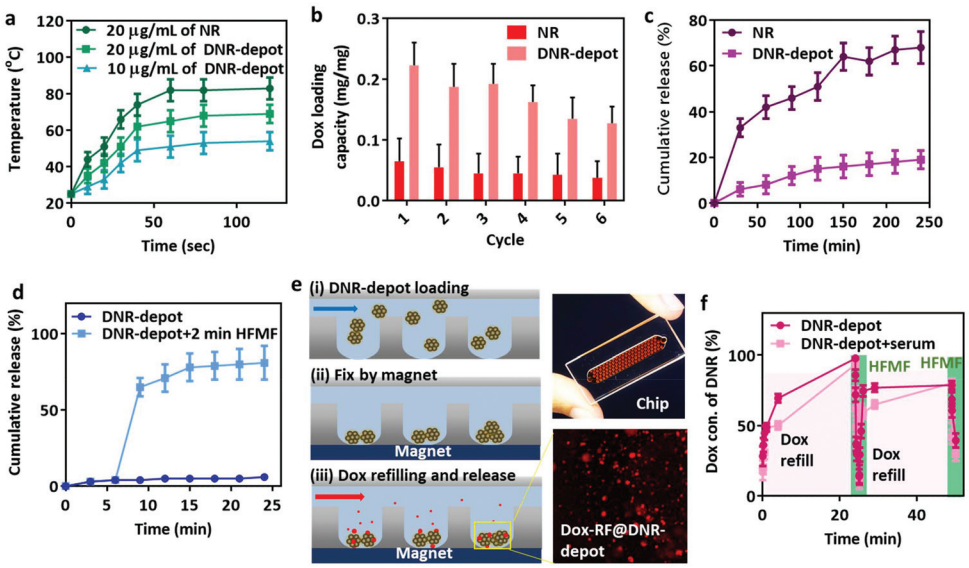

Fig. 4 (a) Thermal heating profile of NRs and DNR-depot after HFMF treatment. (b) Drug loading capacity of NR and DNR-depot under six cycles of refilling and release of Dox. (c) Cumulative release of Dox from DNR-depot and NRs at 37 °C. (d) Dox release profiles from DNR-depot with and without 2 min of HFMF treatment. (e) A schematic illustration of a multiwell microfluidic chip for refilling and releasing DNR-depot. The left panel represents the process of refilling Dox in DNR-depot; the right panel shows a picture of the microfluidic chip and a fluorescence image of DNR-depot on the chip after Dox refilling. (f) Dox release and refilling of DNR-depot after 2 min of HFMF treatment.

could reach 50 °C within 120 s. This fast heating response is convenient for controlled drug release and tumor therapy.

Fig. 4b demonstrates the Dox loading capacity of NR and DNR-depot with repeated heating and loading cycles. In the first cycle, the loading capacities of the DNR-depot and NR were 0.065 and 0.223 mg Dox per mg particle, respectively. The higher loading capacity of DNR-depot was attributed to the strong affinity between DNA and Dox.[34] To estimate the repeated drug release and loading ability, the drug-loaded particles were heated to 50 °C to release most of the Dox and then reloaded into the particles. As shown in Fig. 4b, the loading capacity of DNR-depot gradually decreased, which might have resulted from DNA desorption and fatigue. However, the loading capacity of DNR-depot was maintained at 60% during the sixth cycle.

The Dox release from the NR and DNR-depot was monitored at 37 °C within 240 min (Fig. 4c). Both the Dox release patterns of the NR and DNR-depot were similar but displayed different release rates. Without DNR-depot conjugation, the Dox release rate from the NR was much faster than that from DNR-depot. After 240 min, approximately 70% of Dox was released from the NR. However, the cumulative Dox release from DNR-depot was approximately 18%, indicating that the strong binding between DNA and Dox reduced the release rate. Then, the solution containing 1 wt% DNR-depot was treated with HFMF for 120 s at the sixth minute. In Fig. 4d, after HFMF treatment, a burst release of Dox was observed, and the treatment released more than 50% Dox. The mechanism of rapid release can be understood by the induced heat, which decreased the affinity of hydrogen bonding between Dox and DNA upon reaching a temperature of 42 °C. Even though the HFMF was switched off, Dox release was detected during the following 20 min. Furthermore, the incomplete release was probably led by the interaction between Dox and DNA on the particles.

Having demonstrated the refill process in static solution, a multiwell microfluidic chip was applied to estimate the Dox refill of the DNR-depot in fluid (Fig. 4e). Fabrication of the microfluidic chip made of polydimethylsiloxane (PDMS) was performed according to our previous work.[22] Each chip contained 96 cylindrical wells with widths and depths of 800 and 500 μm, respectively. As shown in Fig. 4e, DNR-depot were loaded into the chip and fixed at the bottom with a magnet. Then, Dox solution at a concentration of 5 μg mL^{-1} was injected into the chip at a constant rate of 100 μL min^{-1} with a syringe pump for 5 min and subsequently washed with 10 mL of deionized water to remove free Dox. The fluorescence images (left bottom panel in Fig. 4e) revealed that the DNR-depot successfully captured Dox, as examined by confocal laser scanning microscopy (CLSM).

The microfluidic chip system was further used to evaluate the Dox refilling and HFMF triggered release in fluid (Fig. 4f). In brief, 20 μg mL^{-1} DNR-depot was fixed on the chip with a magnet and Dox solution (5 μg mL^{-1}) was pumped at a constant rate of 100 μL min^{-1} with a syringe pump. Then, the Dox solution was collected from the chip to estimate the loading of Dox. The results revealed that more than 50% of Dox was absorbed on the DNR-depot within 5 min, and the loading efficiency reached 95% after 24 min. Then, the DNR-depot was treated with 120 s of HFMF at the 24th min. As expected, the rapid release of Dox caused by HFMF was observed during the treatment. Then, the particles were placed into a fresh Dox solution (5 μg mL^{-1}) at the 26th minute. The refilling of Dox into DNR-depot was noticed, and approximately 80% of Dox was able to refill into the particles. Even though HFMF treatment slightly affected the refilling ability due to the heat damage of DNA structures, the rational refilling ability of DNR-depot was potentially applied in further uses. On the other hand, the release and refill could also be carried out in serum solution.

DNR-depot stability in the physiological environment was investigated on a microfluidic chip system, where Dox refilling and HFMF triggered release were carried out in DMEM supplemented with 10% FBS at 37 °C and 5–10% CO_2 to maintain physiological pH. Similar to a previous approach (Fig. 4e), the DNR-depot was fixed at the bottom of a multiwell microfluidic chip with a magnet and Dox solution (5 μg mL^{-1}) was pumped onto the chip with a syringe pump. After refilling, free Dox was collected from the chip to estimate the Dox loading. The physiological environment reduced the Dox refilling efficiency, but the loading efficiency was maintained at 76% after 24 min (see Fig. S3a in ESI†). Furthermore, the refilling process was evaluated after the DNR-depot was preserved in the physiological environment for 10 and 20 days, which decreased the efficiency of Dox refilling from 76% to 68% and 54%, respectively (see Fig. S3b and S3c in ESI†). Although salts and sera affected Dox refilling, more than 50% Dox loading efficiency was still observed, indicating appropriate stability of the DNR in physiological environments. Moreover, a thin layer of chemically bonded DNA was observed on the NR surface after 20 days in a physiological environment (see Fig. S3d in ESI†).

The cytotoxicity of NRs and DNR-depot in RG2 cells (a brain cancer cell line) was estimated by the 3-(4,5-dimethylthiazol-2-yl)-2,5-diphenyltetrazolium bromide (MTT) assay as shown in Fig. 5a. When the concentration of NRs and DNR-depot was less than 4 μg mL^{-1}, the cell viability was higher than 82%, indicating low toxicity. Once the concentration of DNR-depot reached 10 to 20 μg mL^{-1}, approximately 25% of the cells were killed, suggesting the low toxicity of DNR-depot. Then, flow cytometry was used to understand the cell uptake efficiency of the NRs and DNR-depot with RG2 cells, where the particles were labeled with QDs, with fluorescence emission at 600 nm, in the hydrophobic pore for intracellular tracking. As shown in Fig. 5b, the fluorescence intensity (horizontal axis) of RG2 uptake by DNR-depot was approximately 5 times stronger than that of the NRs after 4 h. The improvement in cellular uptake by DNR-depot might be attributed to the unique biosegments of DNA that facilitate cell attachment and internalization.[35,36]

CLSM was performed on RG2 cells incubated with NRs and DNR-depot for 1 and 4 h (Fig. 5c and d). After 1 h of incubation, only a few particles (NR and DNR-depot) shown as red

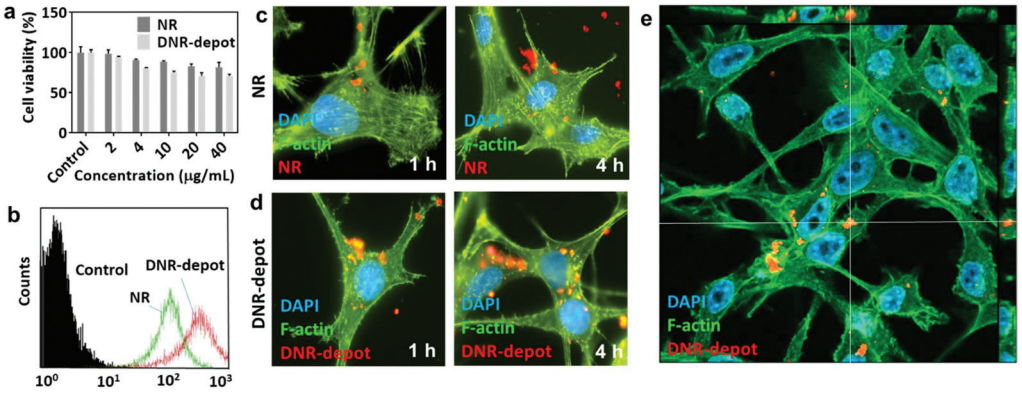

Fig. 5 (a) Cell viability after culturing RG2 cells with NRs and DNR-depot for 24 h. (b) Flow cytometry analysis of NRs and DNR-depot in RG2 cells after incubation for 4 h. CLSM images of the cellular uptake of (c) NRs and (d) DNR-depot at 1 and 4 h. QD-labeled NRs and DNR-depot are represented in red, F-actin from the cells is shown in green, and nuclei (DAPI stained) are shown in blue. (e) CLSM images of RG2 cells incubated with DNR-depot for 4 h.

dots were attached to the cells even though there were no targeting ligands on the particles. With increasing time to 4 h, many DNR-depot were observed around the cell nuclei, but most of the NRs were still attached to the cell membrane, indicating the need for assistance from DNA for cell internalization and natural endocytosis.[35] Furthermore, cross-sections of the CLSM images revealed that DNR-depot was taken up in the cells rather than staying on the surface. The control group of RG2 cells without particle treatment (see ESI, Fig. S4†) showed that the fluorescence signals in Fig. 5c–e were due to the particles.

To evaluate the effects of Dox refilling and release from DNR-depot on cell killing, 20 μg mL^{-1} DNR-depot was placed in the bottom of a transwell at one day postimplantation and 1 × 10^4 RG2 cells were placed in the upper chamber of the transwell (Fig. 6a). After 24 h of incubation, the RG2 cells were attached to the transwell filter of the upper chamber (Fig. 6b). During Dox refilling, the cell chamber was removed temporarily, and 5 μg mL^{-1} Dox was injected into the cell medium for 10 min for DNR-depot loading (see ESI, Fig. S5†). After refilling, the Dox-loaded DNR-depot was fixed by a magnet at the bottom, and the medium was replaced with Dox-free medium. Then, the upper cell chamber of the transwell cell was replaced into the well. The Dox-refilling DNR-depot was termed Dox-RF@DNR-depot. The viability of RG2 cells was then examined by the counting method after another 24 h of treatment. For

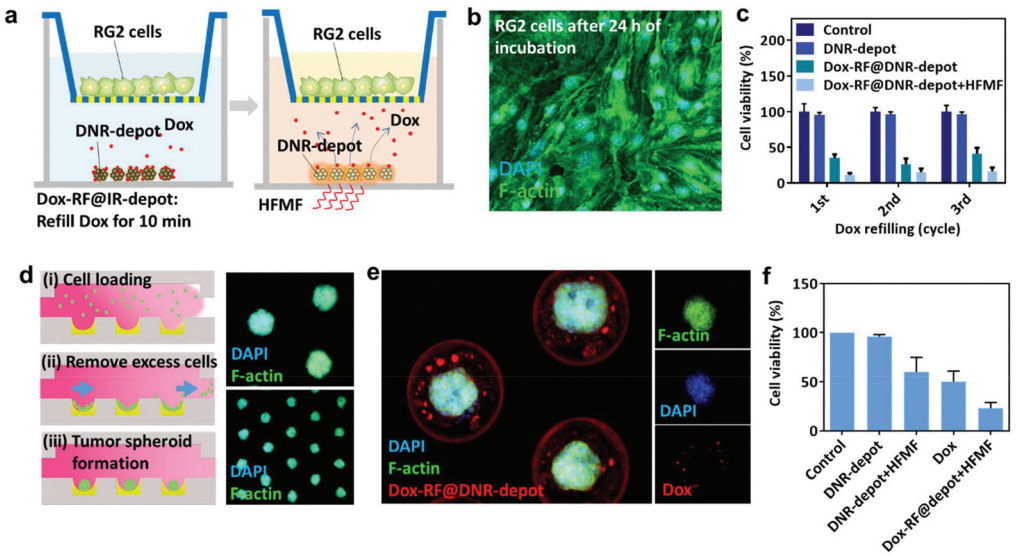

Fig. 6 (a) Schematic illustration of the experimental design for Dox refilling and release of DNR-depot on cell killing. (b) RG2 cells on the upper layer of the transwell after 24 h of incubation. (c) The viability of RG2 cells in the transwell chamber after treatment with DNR-depot, Dox-RF@DNR-depot or Dox-RF@DNR-depot + HFMF for various Dox refilling and release cycles. (d) MTS chip fabricated on a microfluidic chip for the formation of tumor spheroids (left panel). CLSM images of RG2 tumor spheroids on a chip 24 h postinjection. Nuclei are displayed in blue, and F-actin is shown in green (right panel). (e) CLSM image of MTSs treated with DNR-depot and refilling Dox at a fluidic rate of 100 mg ml^{-1} for 2 min. (f) Cell viability of MTSs on a chip after treatment with DNR-depot, DNR-depot + HFMF, Dox or Dox-RF@DNR-depot + HFMF (n = 10).

the HFMF treatment group, the transwell was subjected to 2 min of HFMF 1 h after refilling Dox. Several conclusions can be drawn from the cell killing results (Fig. 6c): (1) During the first cycle, the cell viability of the control and DNR-depot groups was more than 95% after 24 h of incubation since there was no Dox loaded. (2) The cell viability of the Dox-RF@DNR-depot group was less than 40%, revealing that toxic Dox was released from DNR-depot affected cells. (3) In the HFMF treatment group, the cell killing effects were further improved, and approximately 90% of the cells died due to the short duration of high-concentration of Dox. (4) During the second and third cycles, effective cell killing by Dox-RF@DNR-depot was maintained. In these new cycles, nontreated RG2 cells were used, indicating that the DNR-depot drug loading process was successful and cell killing can be achieved for a few cycles.

Having exhibited *in vitro* Dox refilling in cell suppression, the functions of DNR-depot were also evaluated with an *ex vivo* tumor on a chip. By using a similar microfluidic chip and coating with an anti-cell adhesion polymer, the cells were loaded onto the chip (Fig. 6d). Similar to an *in vivo* tumor, dozens of uniform multicellular tumor spheroids (MTSs) exhibiting a heterogeneous and compact multicellular structure can be formed on a chip after 24 h. CLSM images revealed that the resulting MTSs possessed a diameter of approximately 200 μm on average on the chip (right panel of Fig. 6d). At 24 h postincubation of MTSs, 100 μL of DNR-depot (5 μg mL^{-1}) was injected into the chip. After another 4 h, Dox solution (5 μg mL^{-1}) was injected by a syringe pump for 5 min at a constant rate of 100 μL min^{-1}, and subsequently, the free Dox was removed from the chip. The MTSs were fixed and examined by CLSM. The CLSM image in Fig. 6e shows many red fluorescent dots (Dox) on the chip, suggesting the refilling of Dox to the DNR-depot. Upon closer observation, some particles on the MTSs were also able to absorb Dox, indicating the strong affinity between Dox and DNR-depot. Fig. 6f displays the MTS killing effects on a chip. As expected, once the MTSs were treated with DNR-depot, refilled with Dox (Dox-RF) and treated for 2 min with HFMF stimulus, the lowest cell viability was observed due to the combination effects compared with the other treatment groups.

In vivo Dox refilling was conducted by implanting DNR-depot (20 wt%) *via* intratumoral injection. In Fig. 7a, the refilling of Dox was carried out four times on the 2nd, 5th, 14th and 21st days *via* intravenous injection (i.v.) through the tail vein, and the tumors were subjected to HFMF for 20 s at 1 h postinjection to release the captured Dox. To monitor the real-time Dox concentration in the tumor, a tumor-bearing mouse was anesthetized, and then a microdialysis probe (CMA 20 Elite, Stockholm Sweden) was carefully inserted into the tumor. PBS buffer (1 μL min^{-1}) was applied to rinse the microdialysis probe for 2 h, and then, the extracellular fluid was collected by the probe and measured at various time points.

Fig. 7b shows the Dox concentration in the tumor after treatment with various NR or DNR-depot conditions. Several observations were made. First, the Dox concentration in tumors treated with DNR-depot and HFMF was the highest

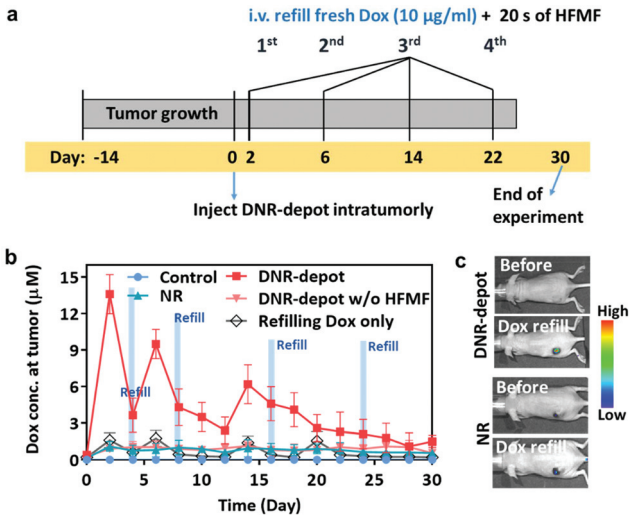

Fig. 7 (a) Treatment schedule of implanting DNR-depot and refilling Dox. (b) Dox concentrations in tumors monitored by microdialysis probes under various treatments. (c) IVIS imaging of tumor-bearing mice before and after DNR-depot and NR Dox refilling. The fluorescence signals of Dox were monitored.

compared to that in the other groups, displaying successful refilling of the Dox into DNR-depot at the tumor site. Second, HFMF treatment exhibited an approximately 8-fold greater Dox concentration from DNR-depot in tumors than without HFMF treatment, *i.e.*, the DNR-depot without HFMF group, during the first cycle. Third, the refilling and release abilities of DNR-depot could be maintained for three cycles over 20 days. However, for the 4th refilling cycle, the Dox concentration at the tumor did not improve, which might be caused by the degradation of the depot DNA and NR. Without implanting DNR-depot, there was only an approximately an 11% Dox refilling concentration compared with that in the DNR-depot group. Overall, the excellent refilling and release of DNR-depot from high concentrations of Dox in tumors for a few weeks revealed the potential to achieve local and effective cell killing. Additionally, the control group was not injected with Dox and did not display Dox signals, indicating a low background signal. IVIS imaging was also used to measure Dox refilling, as shown in Fig. 7c. After Dox refilling, the Dox signal in the DNR-depot group revealed a higher intensity than that in the NR group, which also directly confirmed the refilling ability.

To investigate the antitumor activity, RG2 tumor xenograft mice were intratumorally injected with saline, DNR-depot or NRs and received the following various treatments: (i) control, (ii) DNR-depot, (iii) Dox (i.v. injection *via* tail veins three times), (iv) Dox-RF@DNR-depot, (v) Dox-RF@NR + HFMF, (vi) DNR-depot + HFMF, (vii) Dox-RF@DNR-depot + HFMF and (viii) Dox-1 RF@DNR-depot + HFMF (Dox refilling once at the first treatment). The treatment schedules are shown in Fig. 8a. Dox was refilled on the 2nd, 5th and 14th days *via* intravenous injection (i.v.) through the tail vein. For the HFMF treatment groups, 2 min of HFMF was applied to release Dox and achieve magnetothermal therapy. Fig. 8b shows that the tumors

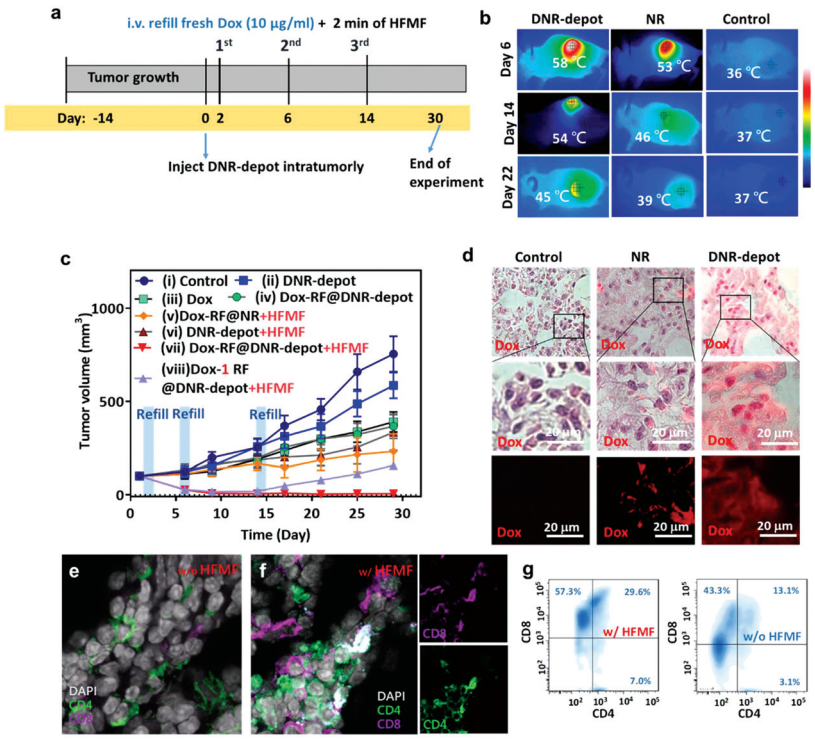

Fig. 8 (a) Treatment schedule of implanting DNR-depot and refilling Dox for tumor inhibition. (b) Infrared thermal images of RG2 tumor-bearing mice under DNR-depot + HFMF and NR + HFMF treatments. (c) Tumor volumes implanting DNR-depot and NRs with or without refilling Dox and HFMF treatment for 30 days. (d) Fluorescence images of tumors one day posttreatment with saline, Dox-RF@NR and Dox-RF@DNR-depot. (e and f) CLSM images of tumors treated with DNR-depot without or with HFMF, where tumor sections were labeled with anti-CD4 and anti-CD8 antibodies. (g) The flow cytometry diagram representing the percentage of CD4 and CD8 T cells in a tumor with or without HFMF treatment.

treated with DNR-depot or NRs can be heated to 58 and 53 °C, respectively, which is acceptable for thermal tumor ablation. Furthermore, on days 14 and 22, the temperature of the tumors treated with DNR-depot or NRs still increased to more than 46 °C. The control group (saline-treated mice) showed no apparent temperature change after treatment.

Tumor inhibition efficiency was monitored for 30 days (Fig. 8c). Upon refilling Dox and applying HFMF, treatment vii with DNR-depot displayed an obvious reduction in tumor size after 30 days. The combination of refilling and thermal chemotherapy was the most effective tumor inhibition treatment. Even with one Dox refilling cycle and HFMF treatment (group viii), the tumor size was reduced within 15 days. However, with drug refilling or HFMF alone, *i.e.*, treatments iv and vi, tumor recurrence was observed after two weeks. Furthermore, compared with treatments v and vii, DNR-depot exhibited better tumor suppression efficacy with DNA assistance than the NR group, suggesting effective Dox refilling in tumor reduction. Overall, DNR-depot is capable of refilling and releasing drugs at tumors to successfully enhance tumor suppression. Furthermore, to evaluate the Dox refilling and release under various treatments upon HFMF, the tumors were collected and evaluated by fluorescence microscopy one day after treatment with saline (control), Dox-RF@NR and Dox-RF@DNR-depot. These three groups were subjected to HFMF to release Dox. As shown in Fig. 8d, DNR-depot exhibited the strongest fluorescence from Dox compared to the other groups, indicating that DNR-depot exhibited the most effective Dox refilling and release into the tumor. These results were consistent with our other findings. On the other hand, the functions of clearance organs, *i.e.*, the liver and kidney, were estimated after 2 days post-Dox refilling in the Dox-RF@DNR-depot (iv) and Dox-RF@DNR-depot + HFMF (vii) groups. Alanine aminotransferase (ALT), alkaline phosphatase (ALP), blood urea nitrogen (BUN), and serum creatinine (CRE) levels were not obviously different from those in the control group (saline), indicating the low toxicity of treatment (see Fig. S6 in ESI†).

The variation of T cells in the tumors was also estimated at two days postimplantation of DNR-depot with and without 2 min of HFMF treatment. Lymphocytes are a critical element for the immune response. After 2 days, the tumors were isolated from the mice, and the populations of cytotoxic and helper T cells in the tumors were evaluated by CLSM and flow cytometry, where the upregulation of T cell surface molecules (CD4 and CD8, typical markers on helper T cells and cytotoxic T cells) was monitored to understand the activity of the immune response. Without HFMF treatment, some cells expressing CD4 and CD8 were observed in the tumor (Fig. 8e). After subjecting the tumor to HFMF, the numbers of cytotoxic T cells and helper T cells were enhanced, suggesting an improvement in T cells actuated by HFMF stimulus (Fig. 8f). Flow cytometry analysis also confirmed this observation

(Fig. 8g). These findings indicated that the DNR-depot and HFMF could be latently used as adjuvants to boost immune therapy.

To estimate the effects on local refilling, DNR-depot was implanted intratumorally, and the refilling Dox process was carried out by injecting Dox directly into the tumor four times on the 2nd, 5th, 14th and 21st days. Then, the tumor inhibition efficacy was monitored for 30 days (see Fig. S7a and S7b in ESI†). The intratumoral Dox-refilling DNR-depot were termed Dox-IT-RF@DNR-depot. Treatment of Dox-IT-RF@DNR-depot with HFMF exhibited an effective tumor suppression efficacy after 30 days. Even when refilling Dox intratumorally only once on the 2nd day, the tumor inhibition efficacy was excellent. Compared to intravenous Dox injection, the Dox concentration of the Dox-IT-RF@DNR-depot at the tumor was approximately 10-fold greater on the sixth day, where the concentration was approximately 91 mM at the tumor, as monitored by a microdialysis probe (CMA 20 Elite, Stockholm Sweden). Furthermore, alanine aminotransferase (ALT), alkaline phosphatase (ALP), blood urea nitrogen (BUN), and serum creatinine (CRE) levels only demonstrated slight differences compared to the control (saline), suggesting low toxicity of treatment (see Fig. S7c in ESI†). Moreover, to further investigate tumor recurrence, the tumor was monitored for 60 days (see Fig. S8 in ESI†). Treatment with both Dox-IT-RF@DNR-depot and Dox-RF@DNR-depot resulted in tumor inhibition and did not exhibit tumor recurrence, suggesting effective therapeutic efficacy for tumor treatment. Moreover, hematoxylin and eosin (H&E) staining of the main organs did not exhibit obvious differences between treated and untreated mice, indicating little influence from the treatments on the major organs (see Fig. S9 in ESI†).

Conclusions

An injectable drug-refilling depot composed of double-strand deoxyribonucleic acid and porous magnetic nanoraspberries has been developed to serve as a drug sponge-like refilling reservoir in tumors. The depot can capture a free anticancer drug (doxorubicin) through the blood, improving the drug concentration by approximately 8-fold compared to that of the free drug alone for 3 refilling cycles. Upon application of a high-frequency external magnetic field (HFMF), large amounts of Dox and intense heat can be generated by the depot, facilitating combination magnetothermal- and chemotherapy. Administration of the depot and drug refilling accomplished excellent *in vivo* tumor inhibition. This depot offers a new injectable strategy for the refilling of drug delivery to tumors, potentially leading to clinical use.

Methods

Synthesis of porous magnetic iron oxide nanoraspberries (NRs)

The NRs were fabricated through a ligand-assisted approach by the coordinating agents oleic amine (OA) and sodium citrate through a hydrothermal reaction.[29] Briefly, 2 mL of OA was added to 20 mL of ethylene glycol (EG, anhydrous, 99.8%, Sigma-Aldrich) to form a clear solution. Then, $FeCl_3{\cdot}6H_2O$ (20 mmol) and anhydrous sodium acetate (NaAc, 40 mmol, Sigma-Aldrich) were added to the mixture and gently stirred to obtain a homogeneous black solution. Then, the mixture was heated to 50 °C for 24 h. Next, the solution was added to a Teflon-lined stainless steel autoclave for hydrothermal reaction at 220 °C for 4, 10 or 24 h. After cooling to 25 °C, the precipitate was washed with ethanol 3 times, and the resulting NRs were collected in ethanol. Before characterization, the NRs were dried under vacuum at room temperature.

Synthesis of DNA-NR (DNR-depot)

To link DNA, 1 mg mL^{-1} NR was redispersed in deionized water (DI water) in advance. Under vigorous stirring at 4 °C, 1-ethyl-3-[3-dimethylaminopropyl]carbodiimide hydrochloride (EDC) and *N*-hydroxysuccinimide (NHS, Sigma-Aldrich) were added for the chemical reaction.[30] Next, an excess of DNA powder (1 mg) was dissolved in PBS buffer (1 ml) with sodium phosphate (10 mM), NaCl (0.15 M), and EDTA (10 mM) at pH 7.2. Then, the NRs (20 mg) were added to 200 μl of imidazole solution (0.1 M, pH 6.0) using PBS buffer as the dilution. Finally, the DNA solution (25 μl) and NR solution (200 μl) were immediately added to a container containing the EDC/NHS reagents (6.52 μmol). After that, the mixture stirred vigorously and 1 ml of the imidazole solution (0.1 M, pH 6.0) was added. The final mixtures were stirred vigorously overnight at 50 °C, excess salt and reactants were removed with PBS buffer and the product was stored at 4 °C in PBS buffer.

Characterizations

The morphology of NR and DNR-depot was analyzed by field emission scanning electron microscope (FE-SEM, JSM-7000F, JEOL, Japan) and transmission electron microscope (JEM-2100, JEOL, Japan). The sample was dried up on silicon wafers with intrinsic configuration and elemental analysis is used by FE-SEM's appendage. The energy-dispersive X-ray spectroscopy (EDS, Oxford-model 6209, Oxford Instruments) was also carried by JSM-7000F. High resolution X-ray photoelectron spectrometer (XPS, ULVAC-PHI Quantera SXM/Auger AES 650, Japan) was used to measure the range of chemical binding energy. Zeta (ζ) potential of particles and dynamic light scattering (DLS, Nano-ZS, Malnern) were estimated the surface charge and size distribution (Zetasizer Nano ZS). X-ray diffractometer (BRUKER, D8 Advance) was used for identification of crystal characteristics of particles. Superconducting quantum interference device (SQUID, Quantum Design MPMS-XL7, USA) from −10 000 G to +10 000 G at 298 K was a magnetometer to detect magnetic fields for magnetic nanomaterial depending on superconducting loops which consisting of two Josephson junctions. Thermogravimetric analyzer (TGA, Seiko SSC 5000, Japan) provide a proportion of each compositions based on differential melting temperature based on physical and chemical properties.

Magnetic thermal heating effect of DNR-depot

Thermal heating of magnetic NR and DNR-depot was actuated by high frequency magnetic field (HFMF, power cube 32/900, President Honor Industries). The concentration of sample is 0.5 mg ml^{-1} applied to altitude of 70% for each time point, and be detected by a thermal couple instantaneously after each time point.

Drug loading and drug encapsulation efficiency

The drug (Dox) loading content (LC%) and drug encapsulation efficiency (EE%) of Dox in DNR-depot and NR were detected by fluorescence spectrophotometer (Hitachi F-7000, Japan) at a wavelength of 590 nm. Fluorescence intensity of released Dox and free Dox are calibrated to concentrations of utilizing standard. Both LC and EE of the drug loaded capacity for particles are calculated by the following equations, respectively. LC% = (weight of the feeding Dox − weight of Dox in the supernatant)/(weight of the particles) × 100%; EE% = (weight of the feeding Dox − weight of Dox in the supernatant)/(weight of the feeding Dox) × 100%.

For *in vitro* drug refilling and release test, Dox-loaded particles were placed into DI water, and then divided into several groups which the concentration was identical. At each time points, the particles were separated by magnet, and then, the 1 mL of supernatant was collected and measured by fluorescence spectrophotometer to determine the Dox amounts. For refilling study, the dox solution was added to the particles mixtures, and then, the free Dox was measured by fluorescence spectrophotometer. Similarly, HFMF-triggered Dox release was carried out by treating the Dox-loading particles with different HFMF treatment conditions. HFMF (power cube 32/900, President Honor Industries) with a frequency of 50 kHz at a strength of 4 kA m^{-1}. After the treatment, a thermometer was also applied to measure the temperature.

Cell culture

The RG2 cells (rat glioblastoma cell line) are maintained in DMEM media supplemented with 10% FBS and 1% penicillin, at 37 °C and in 5% CO_2. The culture media were replaced every two days, and the cells were passaged by trypsinization. When the cells were incubated for 24 h, the various particles were placed to the cells for different concentrations. The cytotoxicity of RG2 cell under different treatments was investigated by using 3-(4,5-dimethylthiazol-2-yl)-2,5-diphenyltetrazolium bromide (MTT agent). Addition of 500 μl of DMEM with RG2 cells at a density of 1.5×10^5 cells per well in 24-well plate incubation for 24 h. Changing a medium in the next day, a range of concentrations of particles were added into each well with 500 μl of total serum-free DMEM and incubation for 24 h under 37 °C. After 24 h, each well are washed with PBS buffer for 2 times and incubated with 10% MTT agent dissolved in dimethyl sulfoxide (DMSO) for 4 h. The absorbance values were detected with a microplate reader (Synergy™ HT Multi-detection microplate reader, BioTek Instruments, Inc. USA) at wavelength of 590 nm to determine the cell viability.

Cellular uptake

For imaging tracking, CdSe quantum dots (QDs) were incorporated into NR or DNR-depot. Briefly, the particles were re-dispersed into 4 ml of *n*-butanol in advance. QDs were added in $CHCl_3$, and the mixture was added with the particles solution. Then, the mixture was vortexed and sonicated for 4 min for QDs loading through hydrophobic interactions. Subsequently, the particles were collected by centrifugation at 7000 rpm, and washed by the excess of ethanol for three times. For the cell uptake experiments, the QDs-labelled particles were cultured to RG2 cells which were cultured on glass coverslips for 24 h in advance. After various culturing time of particles at 37 °C, the medium was removed from the cells, which were washed twice with PBS, fixed for 30 min with 3% formaldehyde (PBS solution). Then, permeabilization was performed with 0.1% Triton X-100 (PBS solution) for 30 min and washed twice with PBS. Finally, the nuclei and actin cytoskeleton were staining with DAPI (1 μg mL^{-1}) and F-actin (300 units mL^{-1}) for 30 min, respectively. The cells were mounted on glass slides and observed by CLSM (Zeiss LSM 800, Germany).

Flow cytometry

In brief, 2 ml of DMEM was added to RG2 cells at a density of 5×10^5 cells in 6-well plate for 24 h of incubation. Then, the QDs-labelled particles were seeded to each well for various time. Then, removing DMEM and washing each well with PBS buffer for 2 times. Subsequently, trypsin–EDTA was added to the culture well to suspend and collect cells. The put the collected cells into Eppendorf with DMEM containing 10% of FBS and 1% of penicillin–streptomycin. The cells are centrifuged at 500 rpm for 10 min, and then collected with PBS. The collected cells are analyzed by flow cytometry (accumulating 10 000 events) to verify the uptake ability of particles.

In vivo experiment

The female BALB/c nude mice about 6–8 weeks were obtained from National Laboratory Animal Center (NLAC) in Taiwan. All animal procedures were performed in accordance with the Guidelines for Care and Use of Laboratory Animals of National Tsing Hua University and approved by the Animal Ethics Committee of National Tsing Hua University. To form a subcutaneous tumor, 1×10^5 of RG2 cells in 100 μL was subcutaneously injected to nude mice. When the tumor volume reached 100 mm^3, 100 μL of saline solution containing 10 wt% of particles was injected at tumor *via* the intratumoral injection. For imaging the Dox in tumor, IVIS Spectrum (IVIS Imaging System 200 Series, Caliper LifeScience, USA) was used (excitation: 420 nm, emission: 520 nm). The tumor sizes and the body weights are measured at each time points after treatment, then calculated the tumor volume by the following equation. All measurements are performed in triplicate. Tumor volume = $(L \times W^2)/2$, where L stands for longest dimension and W is shortest dimension. Relative tumor volume = (v/v'), where v is the tumor volume after treatment, and v' is the initial tumor volume.

In vivo microdialysis experiment

The mouse was anesthetized by isoflurane vaporizer (Matrx VIP3000, MIPMARK), and then the microdialysis probe with a 4 mm-long, 0.5 mm-diameter polyarylethersulfone membrane (molecular weight cut-off: 20 kDa; 8010435, CMA Microdialysis) was carefully inserted into the tumor.[37,38] The perfusion solutions containing 0.9% NaCl or 1.15% KCl were prepared by dissolving their salts in deionized water, freshly obtained from the purification system and were applied to fill the syringes. Before collecting the data, 1 μl min^{-1} of PBS buffer was applied to rinse the microdialysis probe for 2 h. Then, collect the extracellular fluid through the microdialysis probe inserted the mice. The collected solution was then read by microplate reader (Synergy™ HT Multi-detection microplate reader, BioTek Instruments, Inc. USA) at a wavelength of 590 nm to determine the concentrations of dox.

Conflicts of interest

There are no conflicts to declare.

Acknowledgements

This work was financially supported by the Ministry of Science and Technology of the Republic of China, Taiwan under contracts MOST 108-2636-E-007-001 and MOST 107-2636-E-007-002 and by National Tsing Hua University (108Q2510E1) in Taiwan.

References

1 A. R. Town, M. Giardiello, R. Gurjar, M. Siccardi, M. E. Briggs, R. Akhtard and T. O. McDonald, *Nanoscale*, 2017, **9**, 6302.
2 H. Deng, A. Dong, J. Song and X. Chen, *J. Controlled Release*, 2019, **297**, 60.
3 M. Miyazaki, E. Yuba, H. Hayashi, A. Harada and K. Kono, *Bioconjugate Chem.*, 2018, **29**(29), 44.
4 K. Fuchs, R. Duran, A. Denys, P. E. Bize, G. Borchard and O. Jordan, *J. Controlled Release*, 2017, **262**, 127.
5 H. Zhao, J. Xu, J. Wan, S. Geng, H. Li, X. Peng, Q. Fu, M. He, Y. Zhao and X. Yang, *Nanoscale*, 2017, **9**, 5859.
6 I. Kim, W. Y. Bang, W. H. Park, E. H. Han and E. Lee, *Nanoscale*, 2019, **11**, 17327.
7 P. Huang, H. Song, Y. Zhang, J. Liu, Z. Cheng, X. J. Liang, W. Wang, D. Kong and J. Liu, *Biomaterials*, 2017, **145**, 81.
8 P. Huang, X. Wang, X. Liang, J. Yang, C. Zhang, D. Kong and W. Wang, *Acta Biomater.*, 2019, **85**, 1.
9 J. Perry, A. Chambers, K. Spithoff and N. Laperriere, *Curr. Oncol.*, 2007, **14**, 189.
10 N. G. Zaorsky, B. J. Davis, P. L. Nguyen, T. N. Showalter, P. J. Hoskin, Y. Yoshioka, G. C. Morton and E. M. Horwitz, *Nat. Rev. Urol.*, 2017, **14**, 415.
11 Y. W. Jiang, G. Gao, P. Hu, J. B. Liu, Y. Guo, X. Zhang, X. W. Yu, F. G. Wu and X. Lu, *Nanoscale*, 2020, **12**, 210.
12 M. Yin, L. Xiao, Q. Liu, S. Y. Kwon, Y. Zhang, P. R. Sharma, L. Jin, X. Li and B. Xu, *Adv. Healthcare Mater.*, 2019, **8**, 1901170.
13 R. Xing, Y. Liu, Q. Zou and X. Yan, *Nanoscale*, 2019, **11**, 22182.
14 H. Ruan, Q. Hu, D. Wen, Q. Chen, G. Chen, Y. Lu, J. Wang, H. Cheng, W. Lu and Z. Gu, *Adv. Mater.*, 2019, **31**, 1806957.
15 V. V. Vinogradov, A. S. Drozdov, L. R. Mingabudinova, E. M. Shabanova, N. O. Kolchina, E. I. Anastasova, A. A. Markova, A. A. Shtil, V. A. Milichko, G. L. Starova, R. L. M. Precker, A. V. Vinogradov, E. Hey-Hawkins and E. A. Pidko, *J. Mater. Chem. B*, 2018, **6**, 2450.
16 T. Zhang, Y. Tang, W. Zhang, S. Liu, Y. Zhao, W. Wang, J. Wang, L. Xu and K. Liu, *J. Mater. Chem. B*, 2018, **6**, 1216.
17 Y. Li, Y. Niu, J. Zhu, C. Gao, Q. Xu, Z. He, D. Chen, M. Xu and Y. Liu, *Nanoscale*, 2020, **12**, 2673.
18 F. Liu, L. Lin, S. Sheng, C. Xu, Y. Wang, Y. Zhang, D. Wang, J. Wu, Y. Li, H. Tian and X. Chen, *Nanoscale*, 2020, **12**, 1349.
19 Q. Ren, K. Yang, R. Zou, Z. Wan, Z. Shen, G. Wu, Z. Zhou, Q. Ni, W. Fan, J. Hu and Y. Liu, *Nanoscale*, 2019, **11**, 23021.
20 S. Y. Sung, Y. L. Su, W. Cheng, P. F. Hu, C. S. Chiang, W. T. Chen and S. H. Hu, *Nano Lett.*, 2019, **19**, 69.
21 P. Cai, B. Hu, W. R. Leow, X. Wang, X. J. Loh, Y. L. Wu and X. Chen, *Adv. Mater.*, 2018, **30**, 1800572.
22 M. R. Chiang, Y. L. Su, C. Y. Chang, C. W. Chang and S. H. Hu, *Mater. Horiz.*, 2020, **7**, 1051.
23 N. A. Rohner, A. B. Dogan, O. A. Robida and H. A. von Recum, *J. Mater. Chem. B*, 2019, **7**, 5320.
24 Y. Brudno, E. A. Silva, C. J. Kearney, S. A. Lewin, A. Miller, K. D. Martinick, M. Aizenberg and D. J. Mooney, *Proc. Natl. Acad. Sci. U. S. A.*, 2014, **111**, 12722.
25 S. Lee, H. Koo, J. H. Na, S. J. Han, H. S. Min, S. J. Lee, S. H. Kim, S. H. Yun, S. Y. Jeong, I. C. Kwon, K. Choi and K. Kim, *ACS Nano*, 2014, **8**, 2048.
26 J. M. Mejia Oneto, M. Gupta, J. K. Leach, M. Lee and J. L. Sutcliffe, *Acta Biomater.*, 2014, **10**, 5099.
27 Y. Brudno, M. J. Pezone, T. K. Snyder, O. Uzun, C. T. Moody, M. Aizenberg and D. J. Mooney, *Biomaterials*, 2018, **178**, 373.
28 C. Y. X. Chua, P. Jain, A. Ballerini, G. Bruno, R. L. Hood, M. Gupte, S. Gao, N. Di Trani, A. Susnjar, K. Shelton, L. R. Bushman, M. Folci, C. S. Filgueira, M. A. Marzinke, P. L. Anderson, M. Hu, P. Nehete, R. C. Arduino, J. K. Sastry and A. Grattoni, *J. Controlled Release*, 2018, **286**, 315.
29 Y. L. Su, J. H. Fang, C. Y. Liao, C. T. Lin, Y. T. Li and S. H. Hu, *Theranostics*, 2015, **5**, 1233.
30 P. M. Oliver, J. S. Park and D. Vezenov, *Nanoscale*, 2011, **3**, 581.
31 J. H. Lee, J. T. Jang, J. S. Choi, S. H. Moon, S. H. Noh, J. W. Kim, J. G. Kim, I. S. Kim, K. I. Park and J. Cheon, *Nat. Nanotechnol.*, 2011, **6**, 418.
32 S. H. Hu, B. J. Liao, C. S. Chiang, P. J. Chen, I. W. Chen and S. Y. Chen, *Adv. Mater.*, 2012, **24**, 3627.

33 Y. Chao, G. Chen, C. Liang, J. Xu, Z. Dong, X. Han, C. Wang and Z. Liu, *Nano Lett.*, 2019, **19**(7), 4287.
34 P. Zhao, M. Zheng, Z. Luo, X. Fan, Z. Sheng, P. Gong, Z. Chen, B. Zhang, D. Ni, Y. Ma and L. Cai, *Adv. Healthcare Mater.*, 2016, **5**, 2161.
35 S. Huo, H. Li, A. J. Boersma and A. Herrmann, *Adv. Sci.*, 2019, **6**, 1900043.
36 V. Kumar, S. Palazzolo, S. Bayda, G. Corona, G. Toffoli and F. Rizzolio, *Theranostics*, 2016, **6**, 710.
37 C. K. Su and H. H. Tseng, *Mikrochim. Acta*, 2019, **186**, 404.
38 C. K. Su and C. C. Ho, *Anal. Chim. Acta*, 2019, **1055**, 36.